

## High-resolution transmission electron microscopy (HRTEM) study of the 4a and 6a superstructure of bornite $\text{Cu}_5\text{FeS}_4$

YANG DING,<sup>1,\*</sup> DAVID R. VEBLEN,<sup>1</sup> AND CHARLES T. PREWITT<sup>2</sup>

<sup>1</sup>The Morton K Blaustein Department of Earth and Planetary Sciences, Johns Hopkins University, Baltimore, Maryland 21218, U.S.A.

<sup>2</sup>Geophysical Laboratory, Carnegie Institution of Washington, 5251 Broad Branch Road NW, Washington, D.C. 20015, U.S.A.

### ABSTRACT

The crystal structure and microstructure of bornite have been of great interest to mineralogists since the pioneering studies of Morimoto and his colleagues (Morimoto 1964; Koto and Morimoto 1975). Because many questions about bornite remain, we are re-examining its structure using HRTEM. High-resolution transmission electron microscope (HRTEM) images taken along the  $\langle 101 \rangle$  axis of bornite and processed by CRISP show variations of contrast between superstructure images and sublattice (1a) images. This contrast variation in the processed images is assumed to arise from vacancy ordering. Atom coordinates in the 4a-I and 6a-I superstructures are determined with the assumptions that superstructures possess the same symmetry as the sublattice and metal atoms occupy tetrahedral sites. Final structural models of 4a-I and 6a-I superstructures are calculated using simultaneous equations involving structure factors derived from Fourier transforms (FT) of HRTEM images, and the results are confirmed by image and diffraction simulations. With these models, the non-systematic extinctions are explained by the statistical vacancy ordering patterns. However, due to various approximations, the structures proposed are only possible models, but not unique solutions. So far, no low-temperature structure of bornite (2a4a2a) has been observed, but 1a, 2a, and 4a-I or 6a-I superstructure domains are always found to coexist in bornite near room temperature. We have also found that electron beam damage can induce the 1a2a1a superstructure.

### INTRODUCTION

Through X-ray, TEM, and neutron diffraction techniques, the bornite ( $\text{Cu}_5\text{FeS}_4$ )-digenite ( $\text{Cu}_9\text{S}_6$ ) series has been investigated since the study of Frueh (1950). Due to the ordering of vacancies and/or metal atoms during phase transitions, several superstructures (2a, 3a, 4a, 5a, 6a) have been found in this series (see Fig. 1). According to Pierce and Buseck (1978), the superstructures of type I present non-systematic extinctions, whereas superstructures of type II show systematic extinctions. For convenience, all nomenclatures for superstructures of bornite-digenite, such as 2a, 3a, 4a, 5a, 6a, 2a4a2a, adopted in our papers, are consistent with those of Pierce and Buseck (1978). Superstructures are named as multiples of the *a* dimension of the cubic sub-cell (e.g., low bornite = 2a4a2a). Isometric structures are abbreviated by listing only one dimension (e.g., 3a3a3a = 3a). The dimension of each superstructure is a function of temperature and composition. According to previous studies, bornite occurs in three different polymorphs: low-, intermediate-, and high-temperature structural forms. The bornite structure is related to the anti-fluorite structure with sulfur atoms in a face-centered cubic (fcc) substructure and metal atoms (Cu and Fe) distributed among tetrahedral sites. The high-temperature form is stable above 265 °C, and the sulfur atoms form fcc closest packing, whereas the six metal atoms (five Cu and one Fe) and two vacancies are randomly distributed over the eight tetrahedral sites; thus, each tetrahedral site is statistically occupied by 6/8 metal atom. Between 265 and 200 °C, the vacan-

cies and metal atoms are no longer randomly distributed over the tetrahedral sites, but are ordered at particular tetrahedral sites, which doubles the unit cell compared to the high-temperature form (Morimoto and Kullerud 1961). The middle-temperature form can be regarded as derived from the zincblende and anti-fluorite structures by alternating these two cubes along the three crystallographic axes, thus resulting in the 2a superstructure. On cooling below 200 °C, the middle-temperature form is believed to transform to a 2a4a2a superstructure with space group *Pbca* (Koto and Morimoto 1975). In this structure, the vacancies are further ordered along one direction to double the size of the unit cell, compared with that of the middle-temperature structural form. The 4a, 5a, and 6a superstructures can also form with the changes in the Cu/Fe ratio and metal/sulfur ratio at certain temperatures, as shown in Figure 1. Although many efforts (Frueh 1950; Donnay et al. 1958; Kullerud 1960; Morimoto and Kullerud 1961, 1963, 1964; Brett and Yund 1964; Morimoto 1964; Roseboom 1966; Morimoto and Koto 1970; Morimoto and Gyobu 1971; Koto and Morimoto 1975; Putnis and Grace 1976; Putnis 1977; Kanazawa et al. 1978; Pierce and Buseck 1978; Van Dyck et al. 1979, 1980; Posfai and Buseck 1994; Bucur and Berger 1995; Berger and Bucur 1996; Grguric and Putnis 1998, 1999; Grguric et al. 2000) have contributed to determinations of superstructures and phase transition mechanisms, the 3a, 4a, 5a, and 6a superstructures are still unknown. The difficulties in superstructure determination arise from two major problems: (1) the data from X-ray and neutron diffraction are not good enough to confirm calculations, and (2) non-systematic extinction in the diffraction patterns along the  $\langle 101 \rangle$  zone axis (see Fig.

\* E-mail: yding@hpcat.aps.anl.gov

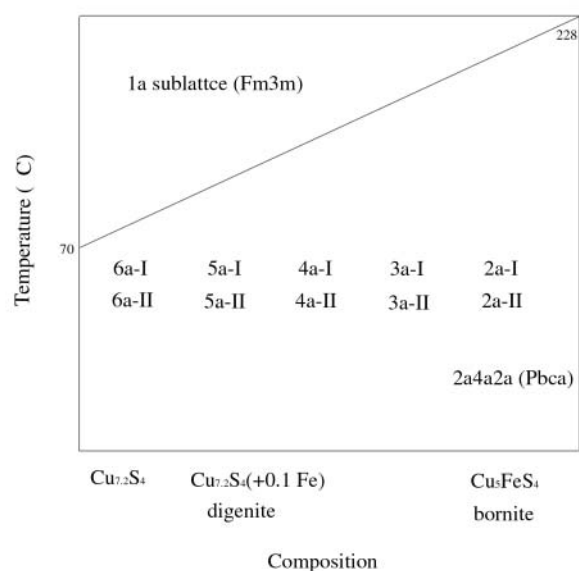


**FIGURE 1.** The approximate composition and temperature ranges for reported bn-dg superstructures (based on Pierce and Buseck 1978). In this figure, the superstructures of type I shows non-systematic extinctions whereas the superstructure of type II shows systematic extinctions.

2) of the superstructures is difficult to explain with diffraction theories. We think the first problem very likely results from the heterogeneity of the bornite-digenite series, although previous authors have not explained in detail why they could not use X-ray or neutron diffraction data to determine superstructures accurately. The second problem causes ambiguity in symmetry determination. To solve the second problem, a twin mechanism (Donnay et al. 1958) and an antiphase domain (APD) boundary mechanism (Putnis and Grace 1976) have been used to explain the anomalous diffraction phenomena. However, TEM work by Pierce and Buseck (1978) found no twin or APD boundaries in superstructures of bornite. Then, using HRTEM images, Pierce and Buseck (1978), Van Dyck (1979, 1980), and Conde et al. (1978) suggested that the nonsystematic extinctions could be caused by vacancy/metal ordering, and Van Dyck (1980) also successfully simulated the optical diffraction patterns of the 5a-I and 6a-I superstructures of digenite with two-dimensional structure models. However, three-dimensional structure models for the superstructures were still not determined. In this paper, by using HRTEM images, image processing, and calculations of structure factors from fast Fourier transforms (FT) of HRTEM images, we propose three-dimensional structure models to explain the nonsystematic extinctions in the 4a-I and 6a-I structures of bornite and the results are confirmed by simulation of HRTEM images and electron diffraction patterns.

## METHODS

### Samples

Bornite samples were obtained from the Mineralogy Department at the Smithsonian National Museum of Natural History. The chosen samples were all euhedral single crystals and were collected from three different locations: (1) Hamley mine, Moonta, South Australia, Australia (NMNH R702); (2) Fairfax quarry, Centerville, Virginia (NMNH 143179); (3) Bristol, Hartford County Connecticut (NMNH

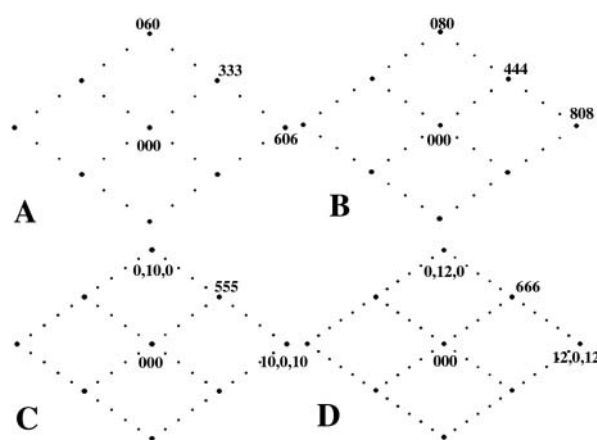


**FIGURE 2.** Schematic diffraction patterns of 3a-I, 4a-I, 5a-I, 6a-I superstructures viewed along the  $[1,0,1]$  axis. (a) diffraction pattern of 3a-I superstructure; (b) diffraction pattern of 4a-I superstructure; (c) diffraction pattern of 5a-I superstructure; (d) diffraction pattern of 6a-I superstructure.

125035). Samples were ground in an agate mortar, suspended in ethanol, and then were dropped on holey carbon grids to make TEM powder samples.

## TEM

All HRTEM images were taken along the  $\langle 101 \rangle$  zone axis of bornite with a Philips CM300 FEG (field emission gun) microscope, operating at 300 kV (TEM mode) or 297 kV [energy-filtered transmission electron microscope (EFTEM) mode], at the Department of Earth and Planetary Sciences, Johns Hopkins University. Images were recorded either on film in TEM mode or with a CCD camera in EFTEM mode. Images recorded with the CCD were easily taken at optimum conditions with the aid of FT of images of the amorphous carbon film calculated with Digital Micrograph software. Images recorded on film usually were not taken exactly under optimum conditions but recorded larger areas compared with those from the CCD camera at the same magnification.

The composition of bornite was obtained from energy-dispersive X-ray spectra (EDS) from the TEM, which were collected and reduced with the ESvision software installed in an EMiSpec analytical system. The quantification of the spectra using the Cliff-Lorimer ratio technique (Cliff and Lorimer 1975; Williams and Carter 1996) was based on the thick film factors of  $K_{FeS}$  and  $K_{CuS}$  that were obtained from a high-quality chalcocopyrite ( $CuFeS_2$ ) standard when the same operation conditions.

## Crystallographic image processing and image simulations

Digitized HRTEM images were processed using crystallographic image processing methods in CRISP (Hovmöller 1992; Zou et al. 1996) to correct for the contrast transfer function (CFT), slight tilt of the sample, and a small degree of astigmatism to obtain two-dimensional projected density maps of atomic potential of the samples. Also, CRISP can test the symmetry of the projected density map and then apply the symmetry to the original image to obtain an ideal HRTEM image. Simulations of HRTEM images and diffraction patterns were obtained using MacTempas software with standard procedures.

## Methods for determination of superstructure models from HRTEM images

Two basic things are needed to determine the structural models: the coordinates of each atom and the occupancy of each metal atom in the superstructures 4a-I and 6a-I. Coordinates of atoms can be obtained from assumed symmetry based on HRTEM images and previous work, and the occupancies of atoms can be determined by approximate mathematical calculations based on FT of HRTEM images. The reason we use FT of HRTEM images rather than direct electron diffraction patterns to calculate the structure factors is that the superstructure domains are too small for the SAED (selected area electron diffraction) method. Even using the smallest selected-area aperture, the weak 5a-I and 6a-I superstructure diffraction spots were never recorded on film, even with long exposure times.

Since the phase shifts of the transmitted electrons caused by phonon excitation in the HRTEM image are minor compared to those from atomic coordinates and occupancies, it is unlikely that the effects of the phonon excitation can be determined from HRTEM images. In this study, the isotropic temperature factors of sulfur and metal atoms were estimated to be  $1.0 (\text{\AA}^2)$  and  $2.5 (\text{\AA}^2)$ , respectively, consistent with the average temperature factors of metal atoms and sulfur in the  $2a$  superstructure of bornite (Kanazawa et al. 1978). Here, all the metal atoms are treated as copper, since copper and iron have very similar X-ray and electron scattering factors (International Tables for Crystallography: Hahn 1996) and the difference between them cannot be distinguished in HRTEM images.

## RESULTS

### Determination of atomic coordinates for $4a$ -I and $6a$ -I superstructures

Figures 3, 4, and 5 show the processed  $1a$ ,  $4a$ -I, and  $6a$ -I images, and they can be regarded as projected density maps (Hovmöller et al. 1992; Zou et al. 1996) of atom potentials from the three-dimensional specimen along the  $\langle 101 \rangle$  zone axis. The bright spots in the processed images correspond to a high density of projected atomic potential (here we use the negative contrast mode in CRISP). Simulation of the  $1a$  structure based on data from Morimoto (1964) indicates that a white spot in the HRTEM image represents one column of

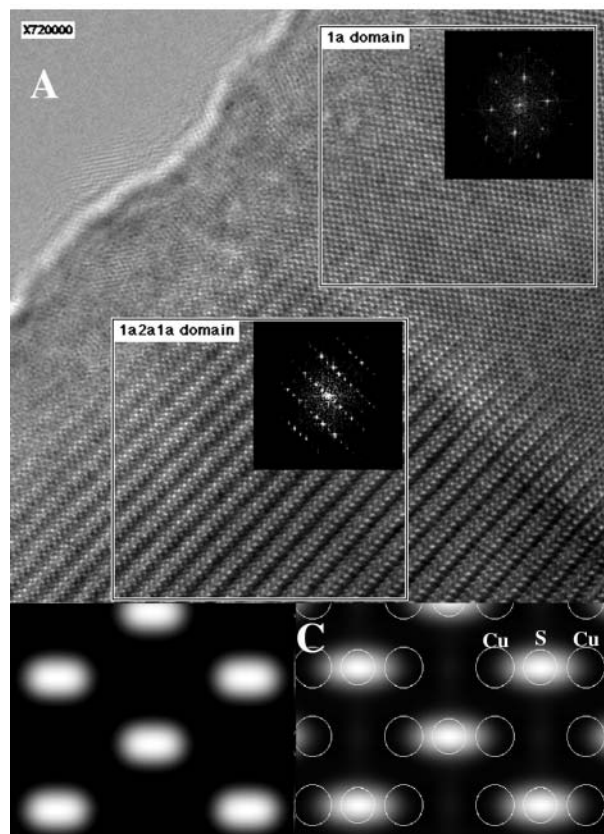


**FIGURE 3.** (a) Experimental HRTEM image of a  $1a$  substructure domain and a  $1a2a1a$  domain in bornite. The  $1a2a1a$  superstructure is introduced by electron-beam irradiation. (b) The  $1a$  substructure processed by CRISP. The white spots represent columns with a high potential projected along a  $\langle 101 \rangle$  direction. (c) The  $1a$  substructure simulated by MacTempas, based on the data of Morimoto (1964). Thickness = 23 nm, defocus = 90 nm.

projected sulfur atoms and two columns of projected metal atoms, as shown in Figure 3. Comparing the superstructures  $4a$ -I and  $6a$ -I with  $1a$  processed HRTEM images, it can be seen that the HRTEM images of superstructures have almost the same geometrical contrast pattern as that of the substructure, except that the spots along the  $\langle 111 \rangle$  directions are brighter. The symmetries of the processed HRTEM images of  $1a$ ,  $2a$ ,  $6a$ -I, and  $4a$ -I (obtained from CRISP) are all  $c2mm$ . Considering the X-ray diffraction results and the space groups with an  $F$  lattice that also have a  $c2mm$  projected plane group along  $\langle 110 \rangle$ , the possible space groups are  $Fm\bar{3}m$ ,  $Fd\bar{3}m$ ,  $F432$ , and  $F4_132$ . To investigate the vacancy/metal ordering mechanism  $Fm\bar{3}m$  was chosen because it made calculations easier. It also can be noticed from the HRTEM images that the coordinates of metal atoms in the  $4a$ -I and  $6a$ -I superstructures are almost the same as those in the  $1a$  and  $2a$  structures, so the metal atoms should occupy the centers of the tetrahedra formed by sulfur atoms. With these assumptions, the coordinates of all atoms in the superstructures  $4a$ -I and  $6a$ -I can be determined as listed in Tables 1 and 2. The remaining question is to determine the occupancies of metal atoms in the superstructures.

### Determination of the metal atom occupancies in the superstructures

The occupancy of each metal atom (or vacancy ordering) can be solved mathematically through FT of HRTEM images. First,

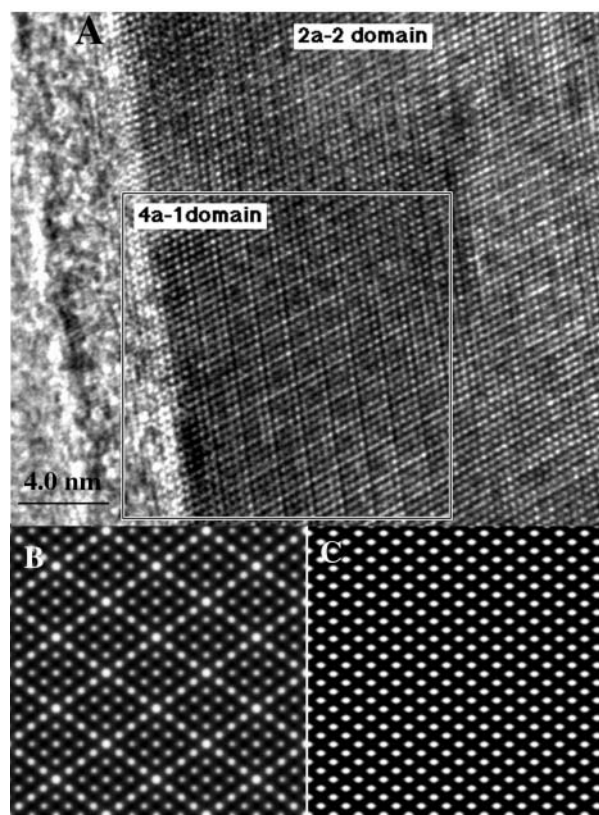


**FIGURE 4.** (a) An experimental HRTEM image of the  $4a$ -I superstructure in bornite recorded on the CCD camera as viewed along  $[1,0,\bar{1}]$ . There are two structure domains,  $4a$ -I and  $2a$ -II, coexisting in this area. (b) The HRTEM image of the  $4a$ -I superstructure domain processed by CRISP. (c) The HRTEM  $1a$  substructure processed by CRISP.

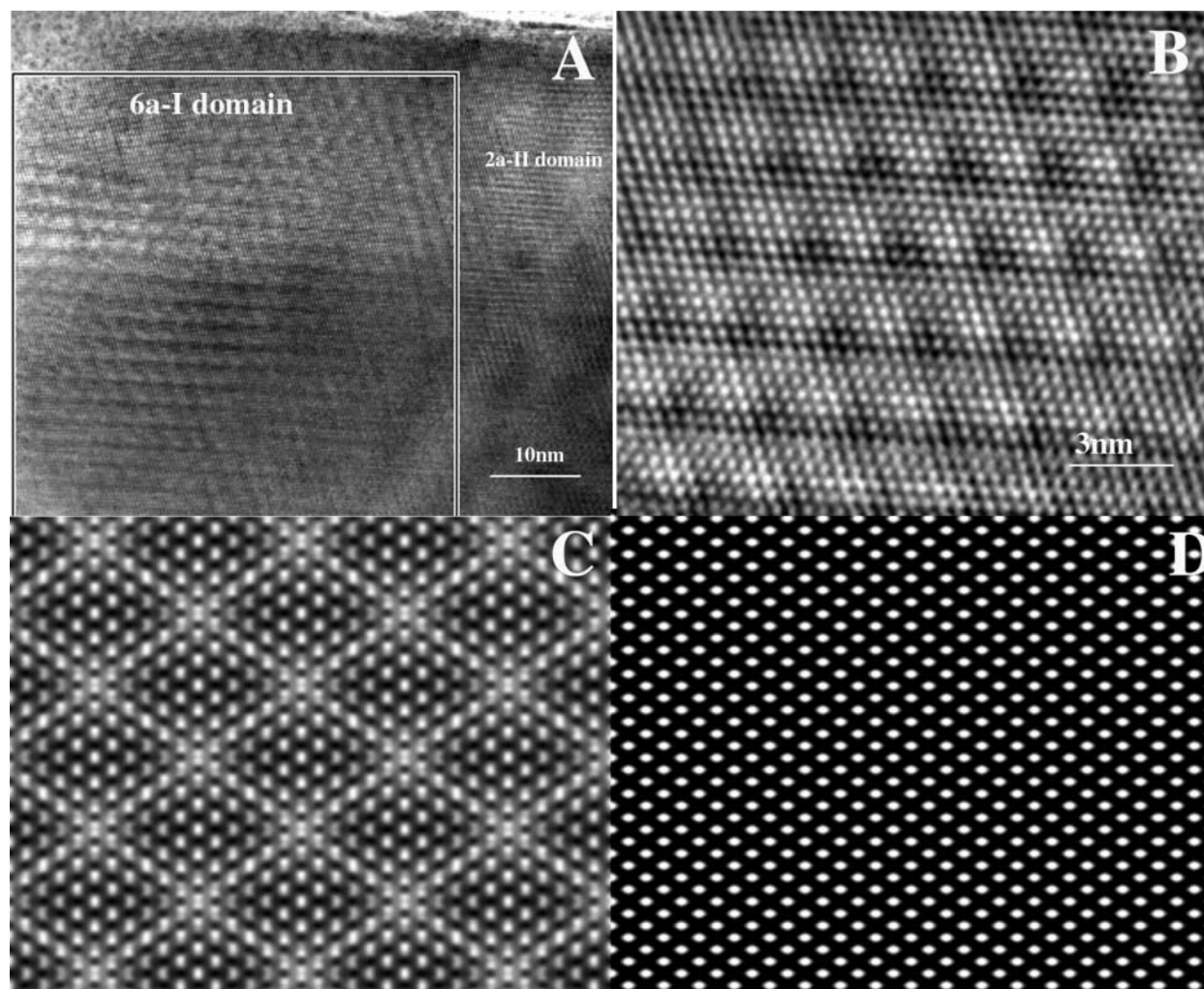


**FIGURE 5.** (a) Experimental HRTEM image of the 6a-I superstructure in bornite recorded on film as viewed along  $[1,0,\bar{1}]$ . (b) The enlarged 6a-I superstructure domain. (c) The processed HRTEM image of the 6a-I superstructure domain. (d) The 1a substructure processed by CRISP.

the intensities of the FT of an HRTEM image can be directly measured by CRISP on the computer. Then, the relationship between the intensity of the FT of HRTEM images and structure factor is derived using weak phase object (WPO) and phase object approximation (POA) imaging theory (Buseck et al. 1992; Williams and Carter 1996). Finally, a group of equations can be obtained from the intensities of FT of HRTEM images to directly calculate the occupancies of the metal atoms. This procedure is similar to X-ray structure determination, except that the coordinates of atoms in this study have already been obtained.

According to the weak phase object (WPO) approximation, the intensity of the FT of an HRTEM image is expressed as

$$I(u) = 2CT(u)|F(u)|$$

(Zou et al. 1996) where  $I(u)$  is the intensity of the FT of the HRTEM image,  $C$  is the interaction constant (equal to  $\pi/\lambda E$ ), and  $F(u)$  is the structure factor of the projected 3-D crystal structure.  $T(u)$  is the phase contrast transfer function (CTF), which describes the perturbation imposed by the TEM instrument on

**TABLE 1.** Structural information for the 4a-1 superstructure model

Atom	x	y	z	B	E	$\sigma$
S	0	0	0	1.0	1	1.0
S	0.25	0	0	1.0	6	1.0
S	0.25	0.25	0	1.0	6	1.0
S	0.125	0.125	0	1.0	12	1.0
S	0.25	0.25	0.25	1.0	2	1.0
S	0.125	0.25	0.125	1.0	24	1.0
S	0.5	0	0	1.0	1	1.0
S	0.375	0.125	0	1.0	12	1.0
Cu/Fe	0.0625	0.0625	0.0625	2.5	8	$\sigma_1$
Cu/Fe	0.1875	0.1875	0.0625	2.5	24	$\sigma_2$
Cu/Fe	0.3125	0.1875	0.0625	2.5	24	$\sigma_3$
Cu/Fe	0.1875	0.0625	0.0625	2.5	24	$\sigma_4$
Cu/Fe	0.3125	0.0625	0.0625	2.5	24	$\sigma_5$
Cu/Fe	0.4375	0.0625	0.0625	2.5	8	$\sigma_6$
Cu/Fe	0.3125	0.1875	0.1875	2.5	8	$\sigma_7$
Cu/Fe	0.1875	0.1875	0.1875	2.5	8	$\sigma_8$

Notes: Symmetry:  $Fm\bar{3}m$ ; cell parameter:  $a = 21.88 \text{ \AA}$ ,  $\sigma$  = undetermined occupancy; E = equivalent sites.

the image phases and can be expressed as (Buseck et al. 1992; Williams and Carter 1996; Zou et al. 1996)

$$T(u) = A(u)\sin \chi(u)$$

**TABLE 2.** Structural information for the 6a-1 superstructure model

Atom	x	y	z	B	E	$\sigma$
S	0	0	0	1.0	1	1.0
S	0.25	0.0833	0	1.0	24	1.0
S	0.3333	0.0833	0.0833	1.0	24	1.0
S	0.3333	0.0000	0.0000	1.0	6	1.0
S	0.4167	0.0000	0.0833	1.0	12	1.0
S	0.5000	0.0000	0.0000	1.0	1	1.0
S	0.0833	0.0833	0	1.0	12	1.0
S	0.1667	0.0833	0.0833	1.0	24	1.0
S	0.2500	0.1667	0.0833	1.0	48	1.0
S	0.3333	0.1667	0.0000	1.0	12	1.0
S	0.1667	0.1667	0.0000	1.0	12	1.0
S	0.2500	0.2500	0.0000	1.0	6	1.0
S	0.1667	0.0000	0.0000	1.0	6	1.0
S	0.1667	0.1667	0.1667	1.0	8	1.0
S	0.2500	0.2500	0.1667	1.0	12	1.0
S	0.1667	0.1667	0.3333	1.0	8	1.0
Cu/Fe	0.0417	0.0417	0.0417	2.5	8	$\sigma_1$
Cu/Fe	0.1250	0.0417	0.0417	2.5	24	$\sigma_2$
Cu/Fe	0.2917	0.2083	0.1250	2.5	24	$\sigma_3$
Cu/Fe	0.2917	0.2083	0.2083	2.5	8	$\sigma_4$
Cu/Fe	0.1250	0.1250	0.1250	2.5	8	$\sigma_5$
Cu/Fe	0.2083	0.1250	0.0417	2.5	24	$\sigma_6$
Cu/Fe	0.1250	0.1250	0.0417	2.5	24	$\sigma_7$
Cu/Fe	0.2083	0.1250	0.1250	2.5	24	$\sigma_8$
Cu/Fe	0.2083	0.0417	0.0417	2.5	24	$\sigma_9$
Cu/Fe	0.2917	0.20833	0.0417	2.5	24	$\sigma_{10}$
Cu/Fe	0.2917	0.0417	0.0417	2.5	24	$\sigma_{11}$
Cu/Fe	0.2083	0.2083	0.0417	2.5	24	$\sigma_{12}$
Cu/Fe	0.3750	0.1250	0.0417	2.5	24	$\sigma_{13}$
Cu/Fe	0.2917	0.1250	0.1250	2.5	24	$\sigma_{14}$
Cu/Fe	0.2083	0.2083	0.1250	2.5	24	$\sigma_{15}$
Cu/Fe	0.4583	0.0417	0.0417	2.5	8	$\sigma_{16}$
Cu/Fe	0.2917	0.1250	0.0417	2.5	48	$\sigma_{17}$
Cu/Fe	0.3750	0.1250	0.1250	2.5	8	$\sigma_{18}$
Cu/Fe	0.3750	0.0417	0.0417	2.5	24	$\sigma_{19}$
Cu/Fe	0.2083	0.2083	0.2083	2.5	8	$\sigma_{20}$

Notes: 6a-1; Symmetry:  $Fm\bar{3}m$ ; cell parameter:  $a = 32.82 \text{ \AA}$ ,  $\sigma =$  undetermined occupancy, E = equivalent sites.

$$A(u) = \exp[-\pi^2 \Delta^2 \lambda^2 u^4 / 2] \times \exp[-\pi^2 \alpha^2 u^2 (\varepsilon + C_s \lambda^2 u^2)]$$

$$\chi(u) = \pi \varepsilon \lambda u^2 + 1/2 (\pi C_s \lambda^3 u^4)$$

where  $A(u)$  is the envelope function of the CTF,  $\Delta$  is the focus spread,  $\alpha$  is the beam divergence, and  $u$  is the vector in reciprocal space. Among those parameters that affect  $T(u)$ , the defocus  $\varepsilon$  is the main parameter changed by the operator during imaging, whereas others are instrumental constants such as  $C_s$ , or vary little from one exposure to the next, as is the case with  $\Delta$  and  $\alpha$ .

To use the FT of the HRTEM image to determine the occupancy of the metal atoms in a 3-D structure, an approximate relationship between the FT of an HRTEM image and the three dimensional structure factors should be estimated first. Based on the POA HRTEM imaging theory, the projected potential of a specimen can be described approximately as  $\phi(x,y) = \int \phi(x,y,z) dz$ . Here,  $\phi(x,y,z)$  is the potential of the specimen when specimen thickness is less than  $100 \text{ \AA}$ , and  $t$  is the thickness of the sample. Using the following approximation, the relationship between FT of an HRTEM image  $[F(h,k)]$  and the three dimensional structure factor  $F(h,k,l)$  can be obtained as

$$\phi(x,y) = \int_0^t \phi(x,y,z) dz = \phi_{\text{average}}(x,y,z) t$$

$$F(h,k,l) = FT[\phi(x,y,z)] \approx FT[\phi_{\text{average}}(x,y,z)] \approx FT\left[\frac{\phi(x,y)}{t}\right] = \frac{F(h,k)}{t}$$

$$F(h,k) \approx F(h,k,l) t$$

The last equation is valid only if  $\phi(x,y,z)$  is rather close to

$\phi_{\text{average}}(x,y,z)$  (averaged structure along the projection direction) at any  $z$ . The more uniform the structure along  $z$  is, the closer the two functions are, and the more reliable the approximate relationship between the  $F(h,k)$  and  $F(h,k,l)$  can be. In this case, the structure contains only three kinds of atoms (copper, iron, and sulfur) with symmetry  $Fm\bar{3}m$ . Thus, the structure is fairly uniform, and the averaged structure along the projection direction would be close to the structure at any  $z$ . However, for structures having more atoms and lower symmetries, the deviation between  $\phi(x,y,z)$  and  $\phi_{\text{average}}(x,y,z)$  may be larger, and the approximation might no longer be valid.

If  $I(u) = 0$  in the FT of the HRTEM image, then either  $T(u)$  or  $F(h,k)$  is equal to 0. The FT of HRTEM images of amorphous materials around the specimen show no dark ring [where the  $T(u) = 0$ ] crossing positions of anomalous diffraction spots. Thus, when  $I(u)$  is equal to zero, that means  $F(u)$  is zero. Therefore, the nonsystematic extinctions in the diffraction pattern along the  $\langle 101 \rangle$  zone axis are thought to arise from  $F(h,k) = 0$ . Based on the relationships above, this means that  $F(h,k,l) = 0$ . Furthermore, the ratio of two intensities in FT of an HRTEM image can be expressed as

$$\frac{I(h_1, k_1)}{I(h_2, k_2)} = \frac{|T(h_1, k_1) F(h_1, k_1)|}{|T(h_2, k_2) F(h_2, k_2)|}$$

and is equal to  $F(h_1, k_1)/F(h_2, k_2)$  since the ratio  $T(h_1, k_1)/T(h_2, k_2)$  is approximately 1 when  $u_1$  and  $u_2$  have similar values. Thus,

$$\frac{I(h_1, k_1)}{I(h_2, k_2)} = \frac{|T(h_1, k_1) F(h_1, k_1)|}{|T(h_2, k_2) F(h_2, k_2)|} = \frac{|F(h_1, k_1)|}{|F(h_2, k_2)|} \approx \frac{|F(h_1, k_1, l_1)|}{|F(h_2, k_2, l_2)|}$$

If the symmetry is  $Fm\bar{3}m$  and  $h = l$ , (i.e., along the  $[1,0,1]$  axis), the structure factor can be simplified to:

$$F(hhk) = 64 \sum_i f_i \sigma_i \{ \cos[2\pi(x_i k)] \cos[2\pi(y_i h)] \cos[2\pi(z_i h)] \\ + \cos[2\pi(y_i k)] \cos[2\pi(z_i h)] \cos[2\pi(x_i h)] \\ + \cos[2\pi(x_i k)] \cos[2\pi(y_i h)] \cos[2\pi(z_i h)] \}$$

Therefore, the intensity or the ratio of intensities of the FT contains only one undetermined variable: the occupancy of the metal site. For the 4a-I superstructure, there are 8 metal atoms, and thus 8 equations are needed and can be found from the FT of a 4a-I HRTEM image (Fig. 6):

$$I(202) = 0 \rightarrow F(202) = 0 \quad (1)$$

$$I(131) = 0 \rightarrow F(131) = 0 \quad (2)$$

$$I(020) = 0 \rightarrow F(020) = 0 \quad (3)$$

$$I(313) = 0 \rightarrow F(313) = 0 \quad (4)$$

$$I(111) = I(333) \rightarrow |F(111)| = |F(333)| \quad (5)$$

$$I(111)I(222) = 1.5 \rightarrow |F(111)| / |F(222)| = 1.5 \quad (6)$$

$$I(222)I(444) = 0.1 \rightarrow |F(222)| / |F(444)| = 0.1 \quad (7)$$

$$(8^* \sigma_1 + 24^* \sigma_2 + 24^* \sigma_3 + 24^* \sigma_4 + 24^* \sigma_5 + 8^* \sigma_6 + 8^* \sigma_7 + 8^* \sigma_8) / 64 = 1.65 \quad (8)$$

The ratio of metal atoms to sulfur atoms in Equation 8, 1.65, was derived from EDS measurements, where  $8^* \sigma_1 + 24^* \sigma_2 + 24^* \sigma_3 + 24^* \sigma_4 + 24^* \sigma_5 + 8^* \sigma_6 + 8^* \sigma_7 + 8^* \sigma_8$  is the total of metal atoms and 64 is the number of sulfur atoms in one unit cell. Solution of these equations using Mathematica 4.0 produced the structure given in Table 3.

For the 6a-I superstructure, there are 20 metal atoms in one

unit cell, but only 18 equations relate intensities in the diffraction pattern (Fig. 7):

- (1)  $I(202) = 0 \rightarrow F(202) = 0$
- (2)  $I(404) = 0 \rightarrow F(404) = 0$
- (3)  $I(131) = 0 \rightarrow F(131) = 0$
- (4)  $I(151) = 0 \rightarrow F(151) = 0$
- (5)  $I(353) = 0 \rightarrow F(353) = 0$
- (6)  $I(535) = 0 \rightarrow F(535) = 0$
- (7)  $I(020) = 0 \rightarrow F(020) = 0$
- (8)  $I(040) = 0 \rightarrow F(040) = 0$
- (9)  $I(242) = 0 \rightarrow F(242) = 0$
- (10)  $I(313) = 0 \rightarrow F(313) = 0$
- (11)  $I(515) = 0 \rightarrow F(515) = 0$
- (12)  $I(424) = 0 \rightarrow F(424) = 0$
- (13)  $I(111) = I(555) \rightarrow |F(111)| = |F(555)|$
- (14)  $I(222) = I(444) \rightarrow |F(222)| = |F(444)|$
- (15)  $I(111) / I(222) = 1.2 \rightarrow |F(111)| / |F(222)| = 1.2$
- (16)  $I(222) / I(333) = 1.2 \rightarrow |F(222)| / |F(333)| = 1.1$
- (17)  $I(333) / I(666) = 0.1 \rightarrow |F(333)| / |F(666)| = 0.1$

$$(8*\sigma_1 + 24*\sigma_2 + 24*\sigma_3 + 8*\sigma_4 + 8*\sigma_5 + 24*\sigma_6 + 24*\sigma_7 + 24*\sigma_8 + 24*\sigma_9 + 24*\sigma_{10} + 24*\sigma_{11} + 24*\sigma_{12} + 24*\sigma_{13} + 24*\sigma_{14} + 24*\sigma_{15} + 8*\sigma_{16} + 48*\sigma_{17} + 8*\sigma_{18} + 24*\sigma_{19} + 8*\sigma_{20}) / 204 = 1.8 \tag{18}$$

Equation 18 is derived from EDS measurements, showing that the metal/sulfur ratio is approximately 1.8. There are 204 sulfur atoms per unit cell, and the number of metal atoms per unit cell is

$$8*\sigma_1 + 24*\sigma_2 + 24*\sigma_3 + 8*\sigma_4 + 8*\sigma_5 + 24*\sigma_6 + 24*\sigma_7 + 24*\sigma_8 + 24*\sigma_9 + 24*\sigma_{10} + 24*\sigma_{11} + 24*\sigma_{12} + 24*\sigma_{13} + 24*\sigma_{14} + 24*\sigma_{15} + 8*\sigma_{16} + 48*\sigma_{17} + 8*\sigma_{18} + 24*\sigma_{19} + 8*\sigma_{20}$$

Thus, the solution is not unique. However, from HRTEM images of the 4a-I and 6a-I superstructures, it appears that the

TABLE 3. Calculated 4a-1 superstructure

Atom	x	y	z	B	σ
Cu/Fe	0.0625	0.0625	0.0625	2.5	1.0
Cu/Fe	0.1875	0.1875	0.0625	2.5	0.9382
Cu/Fe	0.3125	0.1875	0.0625	2.5	0.7882
Cu/Fe	0.1875	0.0625	0.0625	2.5	0.8176
Cu/Fe	0.3125	0.0625	0.0625	2.5	0.7560
Cu/Fe	0.4375	0.0625	0.0625	2.5	0.7264
Cu/Fe	0.3125	0.1875	0.1875	2.5	0.9051
Cu/Fe	0.1875	0.1875	0.1875	2.5	0.6686

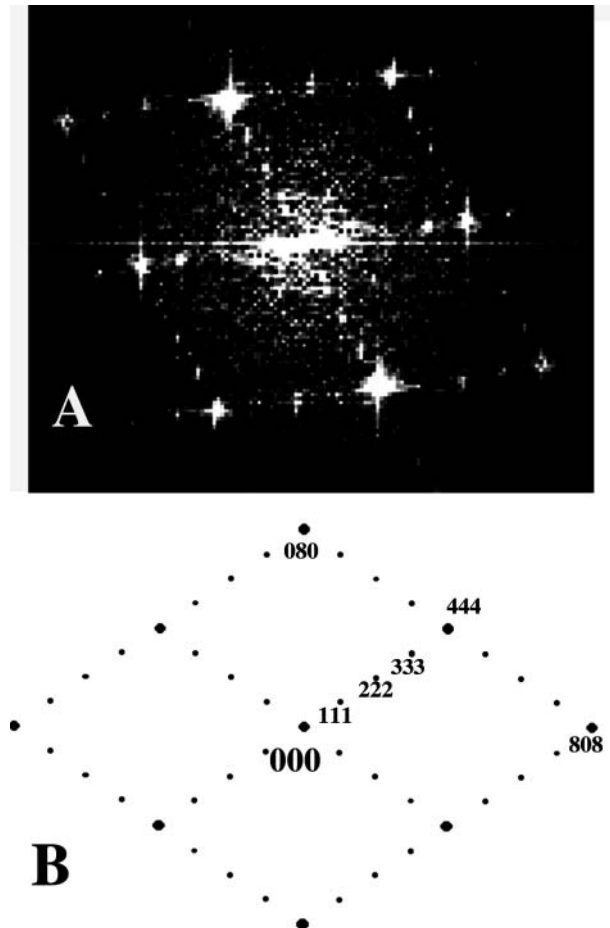


FIGURE 6. (a) FT of a 4a-I superstructure domain calculated using CRISP. (b) Schematic drawing of a 4a-I diffraction pattern viewed along [1,0,1].

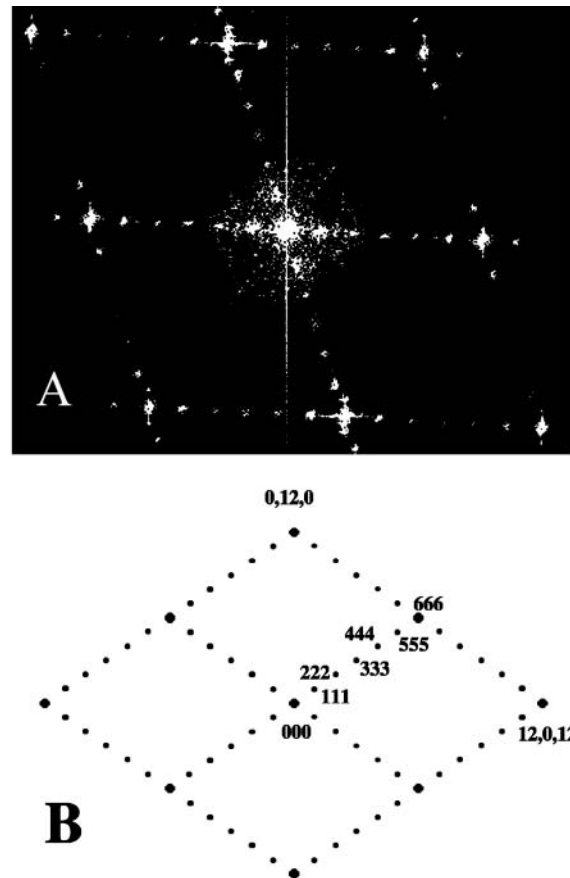


FIGURE 7. (a) FT of HRTEM image from 6a-I superstructure domain. (b) Schematic drawing of a 6a-I diffraction pattern viewed along [1,0,1].

geometry of the ordering of metal atoms and/or vacancies in these two superstructures is analogous, except for the size of the unit cell. Thus, by referring to the 4*a*-I superstructure, we have found that if we set the occupancies of the metal atoms at (0.3750, 0.0417, 0.0417), (0.2917, 0.0417, 0.0417), and (0.4583, 0.0417, 0.0417) to be equal, then the ordering pattern in 6*a*-I is similar to that of 4*a*-I (Fig. 8). This assumption allows calculation of all of the occupancies of metal atoms in the 6*a*-I superstructure (see Table 4).

### Simulations

Simulated HRTEM images and diffraction patterns for the 4*a*-I and 6*a*-I superstructures, calculated by MacTempas, are shown in Figures 9 and 10. The simulation of the HRTEM image and diffraction pattern of 4*a*-I match the experiment extremely well, whereas the simulated HRTEM image for 6*a*-I shows some deviation in contrast from that of the experimental image.

### DISCUSSION

From the results of image and electron diffraction simulations, we conclude that the nonsystematic extinctions for bornite can be caused by variations in the occupancies of the metal atoms, or, in other words, by vacancy ordering. However, some problems still need to be discussed.

### Accuracy of the structure models

In this study, two assumptions and three major approximations have been made for the 4*a*-I and 6*a*-I structural models. The two assumptions are (1) the symmetry of the superstructures is  $Fm\bar{3}m$ , and the metal atoms occupy the centers of the S tetrahedra and (2) Fe and Cu are not ordered in the superstructures. The three approximations are (1)  $F(h,k)$  can be close to  $F(h,k,l)$  when the structure does not change much along the projection direction; (2) the calculation of HRTEM image intensities is under the WPO approximation; and (3) the ratio of metal atoms to sulfur atoms is approximately 1.65 for the 4*a*-I and 1.8 for the 6*a*-I superstructures respectively. For the 6*a*-I superstructure, two additional relationships are estimated, consistent with the solution of the 4*a*-I structure.

TABLE 4. Calculated 6*a*-I superstructure of the 6*a*-I superstructures

Atom	x	y	z	B	$\sigma$
Cu/Fe	0.0417	0.0417	0.0417	2.5	1
Cu/Fe	0.125	0.0417	0.0417	2.5	0.8727
Cu/Fe	0.2917	0.2083	0.125	2.5	0.96
Cu/Fe	0.2917	0.2083	0.2083	2.5	0.9
Cu/Fe	0.125	0.125	0.125	2.5	0.9286
Cu/Fe	0.2083	0.125	0.0417	2.5	0.9023
Cu/Fe	0.125	0.125	0.0417	2.5	0.9558
Cu/Fe	0.2083	0.125	0.125	2.5	0.9250
Cu/Fe	0.2083	0.0417	0.0417	2.5	0.9179
Cu/Fe	0.2917	0.2083	0.0417	2.5	0.9410
Cu/Fe	0.2917	0.0417	0.0417	2.5	0.8434
Cu/Fe	0.2083	0.2083	0.0417	2.5	0.9148
Cu/Fe	0.375	0.125	0.0417	2.5	0.8866
Cu/Fe	0.2917	0.125	0.125	2.5	0.8977
Cu/Fe	0.2083	0.2083	0.125	2.5	0.8195
Cu/Fe	0.4583	0.0417	0.0417	2.5	0.8353
Cu/Fe	0.2917	0.125	0.0417	2.5	0.8814
Cu/Fe	0.375	0.125	0.125	2.5	0.8069
Cu/Fe	0.375	0.0417	0.0417	2.5	0.9167
Cu/Fe	0.2083	0.2083	0.2083	2.5	0.8802

Since the simulation of diffraction matches the experimental diffraction patterns very well, it is clear that  $Fm\bar{3}m$  is consistent with the observations. With this symmetry, the nonsystematic extinctions can now be explained to arise from vacancy/metal ordering. Since it is difficult for HRTEM images and electron diffraction to distinguish Cu/Fe ordering, the second assumption has not been tested in this study. Nevertheless, Fe and Cu have different valence electron and atomic structures, so that they should display differences in bonding with S atoms. Thus, it is likely that Fe/Cu are ordered in low temperature forms.

The assumptions made in this study affect the accuracy of the calculated occupancy for each metal atom. Though an approximate relationship is assumed between the FT of HRTEM images and three dimensional structure factors, the deviation

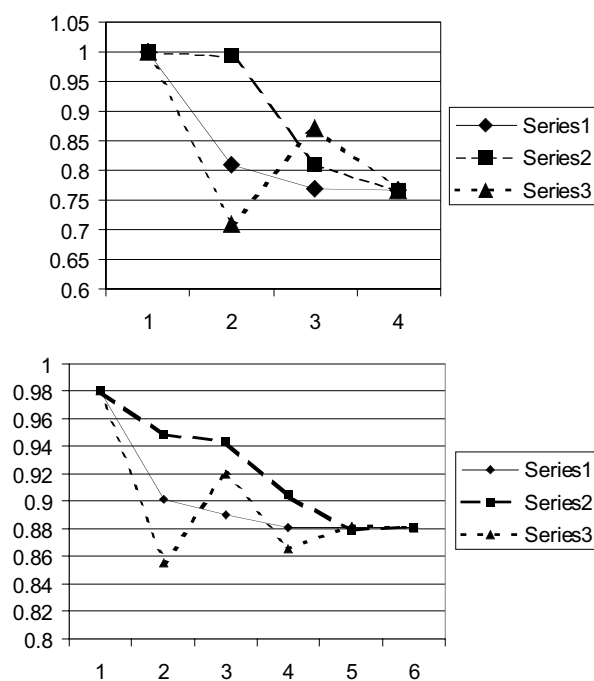
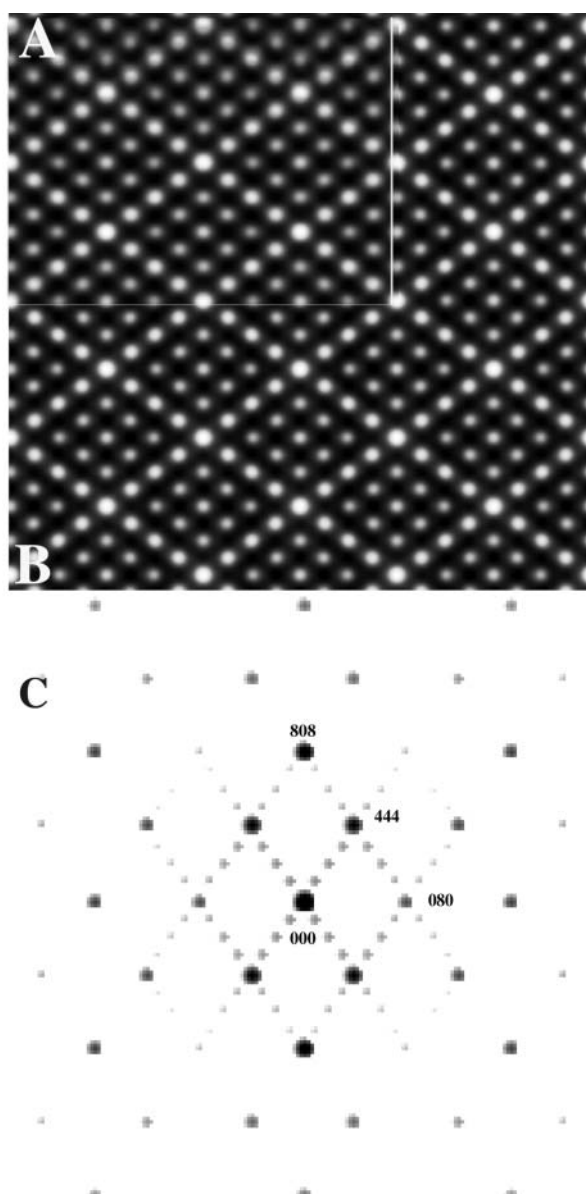
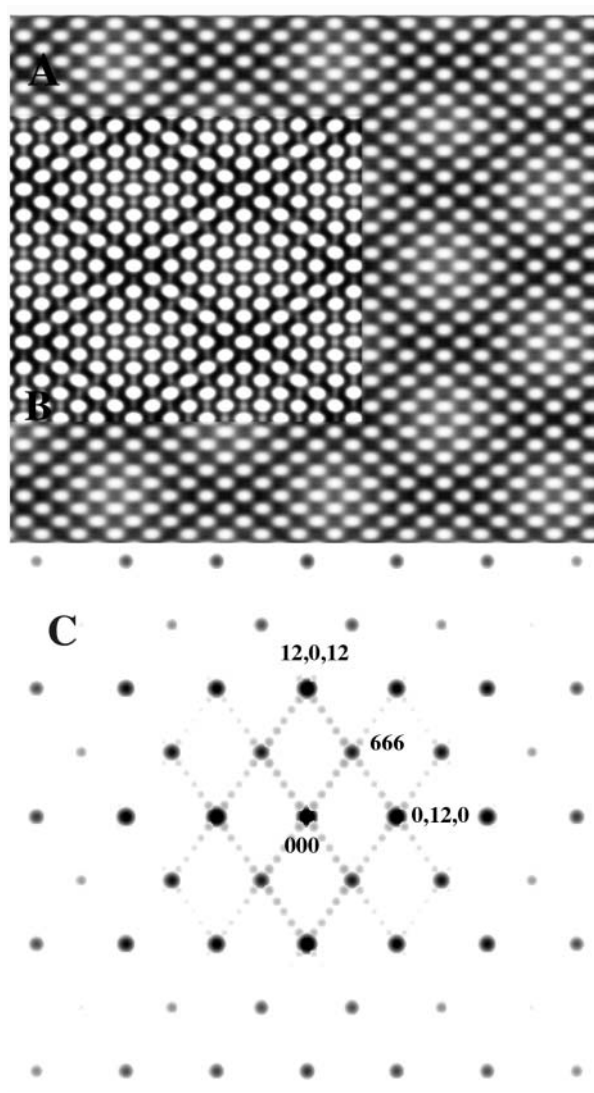


FIGURE 8. Graphs showing the ordering patterns of the 4*a*-I and 6*a*-I superstructures. The series 1 plots represent the ordering along  $\langle 100 \rangle$ ; series 2 plots represent the ordering along  $\langle 101 \rangle$ ; series 3 plots represent ordering along  $\langle 111 \rangle$ . (a) Ordering pattern of the 4*a*-I superstructure. The series 1 plot represents the metal atoms at sites 1: (0.0625, 0.0625, 0.0625); 2: (0.1875, 0.0625, 0.0625); 3: (0.3125, 0.0625, 0.0625); 4: (0.4375, 0.0625, 0.0625). The series 2 plots represent metal atoms at sites 1: (0.0625, 0.0625, 0.0625); 2: (0.1875, 0.1875, 0.0625); 3: (0.3125, 0.1875, 0.0625); 4: (0.4375, 0.0625, 0.0625). The series 3 plots represent the metal atoms at sites 1: (0.0625, 0.0625, 0.0625); 2: (0.1875, 0.1875, 0.1875); 3: (0.3125, 0.1875, 0.1875). (b) Ordering pattern of 6*a*-I superstructure. The series 1 plots represent the metal atoms at sites 1: (0.0417, 0.0417, 0.0417); 2: (0.1250, 0.0417, 0.0417); 3: (0.2083, 0.0417, 0.0417); 4: (0.2917, 0.0417, 0.0417); 5: (0.3750, 0.0417, 0.0417); 6: (0.4583, 0.0417, 0.0417). The series 2 plots represent the metal atoms at sites 1: (0.0417, 0.0417, 0.0417); 2: (0.1250, 0.0417); 3: (0.2083, 0.2083, 0.0417); 4: (0.2917, 0.2083, 0.0417); 5: (0.3750, 0.1250, 0.0417); 6: (0.4583, 0.0417, 0.0417). The series 3 plots represent the metal atoms at sites 1: (0.0417, 0.0417, 0.0417); 2: (0.1250, 0.1250, 0.1250); 3: (0.2083, 0.2083, 0.2083); 4: (0.2917, 0.2083, 0.2083); 5: (0.3750, 0.1250, 0.1250); 6: (0.4583, 0.0417, 0.0417).



**FIGURE 9.** (a) Simulated HRTEM image of the  $4a$ -I superstructure viewed along  $[1,0,\bar{1}]$ . Thickness = 5 nm, defocus = -90 nm; (b) Processed experimental image of the  $4a$ -I superstructure viewed along  $\langle 101 \rangle$ ; (c) The simulated diffraction pattern viewed along  $[1,0,\bar{1}]$ .

between  $\varphi(x,y,z)$  and  $\varphi_{\text{average}}(x,y,z)$  certainly has introduced errors in the calculated structures. However, due to the lack of decent electron or X-ray diffraction data, this may be the only way to approximate the structure factors. Conditions for the WPO approximation require that the sample thickness be below 50 Å, but, in our study, the sample thickness is about 150–200 Å. Thus, the final structure models for  $4a$ -I and  $6a$ -I cannot be completely accurate. Moreover, as pointed out by Van Dyck (1996), the linear relationship between projected potentials and contrast of image may not be reliable due to the possible channeling effect along the zone axis for even very thin samples. Thus, errors may be introduced into the occupancy calculation by using



**FIGURE 10.** (a) Simulated HRTEM image of the  $6a$ -I superstructure viewed along  $[1,0,\bar{1}]$ . Thickness = 20 nm, defocus = 50 nm; (b) Processed image of the  $6a$ -I superstructure viewed along  $\langle 101 \rangle$ ; (c) The simulated diffraction pattern viewed along  $[1,0,\bar{1}]$ .

linear approximation to approach the non-linear problems. As for the chemical compositions of superstructures  $4a$ -I and  $6a$ -I, our EDS measurements indicate that the metal/sulfur ratios are around 1.65 and 1.8. However, the compositions measured by EDS in the TEM are likely to be in error by about 5%. In addition, electron-beam irradiation for long times (e.g., 100 s) can produce compositional changes in the sample. Thus, the results of the calculation may be affected by the errors in the composition measurements.

From the previous discussion, the structure models calculated here are clearly only an approximation; it is hoped that they can eventually be refined using other methods. However, in spite of any inaccuracy, the structure models successfully indicate that the nonsystematic extinctions can arise from vacancy ordering, if the symmetry of superstructures  $4a$ -I and  $6a$ -I is  $Fm\bar{3}m$ .

### Questions about the low structural form of bornite and the heterogeneity of superstructures

Thus far, we have not observed the expected low structural form of bornite:  $2a4a2a$  ( $Pbca$ ), but we find that the  $1a$  and  $2a$  domains coexist with the  $4a$ -I or  $6a$ -I domains at room temperature. The FT of HRTEM images containing  $1a$ ,  $2a$ , and  $4a$  domains look like previous diffraction patterns for the  $2a4a2a$  superstructure. In previous TEM work, only Pierce and Buseck (1978) showed HRTEM images of the  $2a4a2a$  low form of bornite, but no diffraction patterns or FT of images were presented to confirm this result. The samples that we investigated are all heterogeneous, and it is always seen that  $1a$  and  $2a$  domains exist in the samples, even at room temperature. Furthermore, the  $4a$ -I and  $6a$ -I domains are commonly observed to coexist with  $2a$  and  $1a$  domains, but they don't coexist with each other, and the most frequently observed microstructures involve coexistence of  $2a$  and  $4a$  phases. Another discrepancy with previous work is the observation that the  $4a$ -I and  $6a$ -I superstructures can exist in bornite and not digenite. The samples we have studied strongly suggest that bornite is characterized by structural heterogeneity, and this heterogeneity is probably the primary reason why X-ray and neutron diffraction have not solved all of the issues concerning the bornite structures. It is likely that any X-ray or neutron diffraction study will determine only an average structure, not the true structure of the superstructure domains.

### Symmetry ambiguity and modulation mechanism

Though structural models with symmetry  $Fm\bar{3}m$  can explain anomalous diffraction (i.e., nonsystematic extinctions), this symmetry may not be unique if considered from the view of the mathematical model. Using the same methods as above, three other space groups,  $Fd\bar{3}m$ ,  $F432$ , and  $F4_132$ , may also produce the anomalous diffraction patterns. Thus, ambiguity in the symmetry still exists and needs further investigation. The structural models can only indicate that there are certain geometries of the scattering powers of metal sites in bornite satisfying the conditions to produce the non-systemic extinction diffraction. In fact, the geometry of the scattering powers of metal sites could be caused by metal/vacancy ordering, but it also could be caused by other modulation mechanisms, such as bonding effects, which should also be explored.

### ACKNOWLEDGMENT

The bornite single crystals were kindly provided by Department of Mineral Sciences, National Museum of Natural History, Smithsonian Institution. This research was supported by NSF grants EAR0073955 and EAR0409071

### REFERENCES CITED

- Berger, R. and Bucur, R.V. (1996) Potentiometric measurements of copper diffusion in polycrystalline chalcocite, chalcopyrite and bornite. *Solid State Ionics*, 89, 269–278.
- Brett, R. and Yund, R.A. (1964) Sulfur-rich bornites. *American Mineralogist*, 49, 1084–1098.
- Bucur, R.V. and Berger, R. (1995) Electrochemical potentiometric determination of the diffusion coefficient of copper in low digenite, a copper sulfide. *Solid State Ionics*, 76, 291–296.
- Buseck, P.R., Cowley, J.M., and Eyring, L. (1992) *High-Resolution Transmission Electron Microscopy and Associated Techniques*. Oxford University Press, New York.
- Cliff, G. and Lorimer, G.W. (1975) The quantitative analysis of thin specimens. *Journal of Microscopy*, 103, 203–207.
- Conde, C., Manolikas, C., Van Dyck, D., Delavignette, P., Van Landuyt, J., and Amelinckx, S. (1978) Electron microscopic study of digenite-related phases ( $Cu_2S$ ). *Materials Research Bulletin*, 13, 1055–1063.
- Donnay, G., Donnay, J.D.H., and Kullerud, G. (1958) Crystal and twin structure of digenite,  $Cu_5S_5$ . *American Mineralogist*, 43, 228–242.
- Frueh, A.J., Jr. (1950) Disorder in the mineral bornite,  $Cu_3FeS_4$ . *American Mineralogist*, 35, 185–192.
- Grguric, B.A. and Putnis, A. (1998) Compositional controls on phase-transition temperatures in bornite: a differential scanning calorimetry study. *Canadian Mineralogist*, 36, 215–227.
- — — (1999) Rapid exsolution behavior in the bornite-digenite series, and implication for natural ore assemblages. *Mineralogical Magazine*, 63, 1–12.
- Grguric, B.A., Harrison, R.J., and Putnis, A. (2000) A revised phase diagram for the bornite-digenite join from in-situ neutron diffraction and DSC experiments. *Mineralogical Magazine*, 64, 213–231.
- Hahn, T. (1996). *International Tables for Crystallography*. Kluwer Academic Publishers, Dordrecht.
- Hovmöller, S. (1992) CRISP: crystallographic image processing on a personal computer. *Ultramicroscopy*, 41, 121–135.
- Kanazawa, Y., Koto, K., and Morimoto, N. (1978) Bornite ( $Cu_3FeS_4$ ): stability and crystal structure of the intermediate form. *Canadian Mineralogist*, 16, 397–404.
- Koto, K. and Morimoto, N. (1975) Superstructure investigation of bornite,  $Cu_3FeS_4$ , by the modified partial Patterson function. *Acta Crystallographica*, B31, 2268–2273.
- Kullerud, G. (1960) The  $Cu_5S_5$ - $Cu_3FeS_4$  join. *Carnegie Institution of Washington Year Book*, 59, 114–116.
- Morimoto, N. (1964) Structures of two polymorphic forms of  $Cu_3FeS_4$ . *Acta Crystallographica*, 17, 351–360.
- Morimoto, N. and Gyobu, A. (1971) The composition and stability of digenite. *American Mineralogist*, 56, 1889–1909.
- Morimoto, N. and Koto, K. (1970) Phase relations of the Cu-S system at low temperatures: stability of anilite. *American Mineralogist*, 55, 106–117.
- Morimoto, N. and Kullerud, G. (1961) Polymorphism in bornite. *American Mineralogist*, 46, 1270–1282.
- — — (1963) Polymorphism in digenite. *American Mineralogist*, 48, 110–123.
- — — (1964) Polymorphism on the  $Cu_3FeS_4$ - $Cu_5S_5$  join. *Zeitschrift für Kristallographie*, 123, 235–254.
- Pierce, L. and Buseck, P.R. (1978) Superstructuring in the bornite-digenite series: a high resolution electron microscopy study. *American Mineralogist*, 63, 1–16.
- Posfai, M. and Buseck, P.R. (1994) Djurleite, digenite, and chalcocite: intergrowths and transformations. *American Mineralogist*, 79, 308–315.
- Putnis, A. (1977) Electron diffraction study of phase transformation in copper sulfides. *American Mineralogist*, 62, 107–114.
- Putnis, A. and Grace, J. (1976) The transformation behavior of bornite. *Contributions to Mineralogy and Petrology*, 55, 311–315.
- Roseboom, E.H.J. (1966) An investigation of the system Cu-S and some natural copper sulfides between 25C and 700C. *Economic Geology*, 61, 641–672.
- Van Dyck, D. and Op de Beeck, M. (1996) A simple intuitive theory for electron diffraction. *Ultramicroscopy*, 64, 99–107.
- Van Dyck, D., Conde, C., and Amelinckx, S. (1979) The diffraction pattern of crystals presenting a digenite type of disorder I. *Physica Status Solidi*, 56, 327–334.
- Van Dyck, D., Conde-Amiano, C., and Amelinckx, S. (1980) The diffraction pattern of crystals presenting a digenite type of disorder II. *Physica Status Solidi*, 58, 451–468.
- Williams, D.B. and Carter, C.B. (1996) *Transmission Electron Microscopy*. Plenum Press, New York and London.
- Zou, X., Sundberg, M., and Hovmöller, S. (1996) Structure projection retrieval by image processing of HRTEM images taken under non-optimum defocus conditions. *Ultramicroscopy*, 62, 103–121.

MANUSCRIPT RECEIVED OCTOBER 14, 2003

MANUSCRIPT ACCEPTED FEBRUARY 11, 2005

MANUSCRIPT HANDLED BY BERTRAND DEVOUARD